RESEARCH

Multiplexing near- and far-field functionalities with high-efficiency bi-channel metasurfaces

Changhong Dai[1†], Tong Liu[2†] ⬤, Dongyi Wang[3*] ⬤ and Lei Zhou[1,4*]

[†]Changhong Dai and Tong Liu are equally contributed to this work.

*Correspondence:
phwang@hkbu.edu.hk;
phzhou@fudan.edu.cn

[1] State Key Laboratory of Surface Physics, Key Laboratory of Micro and Nano Photonic Structures (Ministry of Education) and Department of Physics, Fudan University, 200438 Shanghai, People's Republic of China
[2] Department of Physics, The Hong Kong University of Science and Technology, Clear Water Bay, Kowloon, Hong Kong, China
[3] Department of Physics, Hong Kong Baptist University, Kowloon Tong, Hong Kong, China
[4] Shanghai Key Laboratory of Metasurfaces for Light Manipulation, 200433 Shanghai, People's Republic of China

Abstract

Propagating waves and surface waves are two distinct types of light-transporting modes, the free control of which are both highly desired in integration photonics. However, previously realized devices are bulky in sizes, inefficient, and/or can only achieve one type of light-manipulation functionality with a single device. Here, we propose a generic approach to design bi-channel meta-devices, constructed by carefully selected meta-atoms possessing reflection phases of both structural-resonance and geometric origins, which can exhibit two distinct light-manipulation functionalities in near-field (NF) and far-field (FF) channels, respectively. After characterizing the scattering properties of basic meta-atoms and briefly stating the theoretical strategy, we design/fabricate three different meta-devices and experimentally characterize their bi-channel wave-control functionalities in the telecom regime. Our experiments show that the first two devices can multiplex the generations of NF and FF optical vortices with different topological charges, while the third one exhibits anomalous surface plasmon polariton focusing in the NF and hologram formation in the FF simultaneously. Our results expand the wave-control functionalities of metasurfaces to all wave-transporting channels, which may inspire many exciting applications in integration optics.

Keywords: Bi-channel metasurfaces, Near-field (NF) channels, Far-field (FF) channels, Integration photonics, Structural-resonance, Geometric phase, Optical vortice, Surface plasmon polariton, Hologram

Introduction

As an important information carrier, light can either propagate in three-dimensional free space as a propagating wave (PW), or be bounded to a dielectric/metal interface moving as a surface wave (SW) [1–3]. PW and SW represent two distinct types of light-transporting modes in the far-field (FF) and near-field (NF) channels, respectively, both have been extensively exploited in the past years for information convey or matter-property probing [3]. Controlling PWs and SWs in the desired manners are thus crucial for photonics research and applications. For example, manipulating light in the FF channel is the basis for applications such as remote sensing [4, 5], optical communications [6–8], optical manipulation [9] and imaging systems [10], while

controlling light at the NF is highly desired in on-chip photonic applications including super-resolution imaging [11–13], bio-sensing [14–17] and nano-lasing [18–20]. However, optical devices made by naturally existing materials are typically bulky in sizes and exhibit limited functionalities, due to weak light-matter interactions and lack of magnetic responses at optical frequencies.

Metasurfaces, planar metamaterials constructed by sub-wavelength microstructures exhibiting tailored scattering properties arranged in certain global sequences, were found to exhibit extraordinary capabilities of light manipulation. By engineering the reflection/transmission phases of individual meta-atoms and their global arrangement sequences, many fascinating wave-manipulation effects in either the FF region (e.g., polarization controls[21–25], anomalous transmissions/reflections[26–28], generations of complex vectorial optical fields[29, 30]) or the NF region (e.g., perfect conversion between PW and SW[1, 2, 31, 32], high-efficiency manipulations on SWs[33–37], etc.) have been realized based on metasurfaces. Moreover, constructed with meta-atoms possessing tailored optical responses with respect to differently polarized incident light, multifunctional metasurfaces were realized to exhibit predesigned wave-manipulation functionalities as shined by light with different polarizations[38–51]. Yet, though numerous efforts have been devoted to enrich the functionalities of multi-functional meta-devices (say, extending the excitation polarizations from linear polarizations[38–42] to circular ones[43–49]), meta-devices realized so far can only control light in one single channel (i.e., either the FF or the NF channel), wherein different functionalities may interfere with each other due to their possible spatial overlaps, as the meta-devices are shined by light with an arbitrary polarization. Further considering the fact that both FF and NF capabilities are important for photonic applications, these meta-devices, working only on one of the two distinct light-propagating modes, are certainly unfavourable for future integration-optics applications. Though attempts have been made to multiplex wave-control functionalities in NF and FF channels into one device[52], employing geometric phases only without a clear design strategy, the realized meta-devices exhibited limited and spin-locked bi-functionalities in two channels.

In this article, we propose a generic strategy to design bi-channel metasurfaces and experimentally demonstrate that such meta-devices can exhibit distinct wave-control functionalities in the two channels at telecom wavelengths. Designing a set of meta-atoms exhibiting spin-delinked reflection phases dictated by both structural-resonance and Pancharatnam−Berry (PB) mechanisms[53–55], we employ them to realize bi-channel metasurfaces possessing two distinct phase distributions enabling independent wave-control functionalities in the NF and FF regions under two spin-polarized incidences, respectively. In particular, the phase profile corresponding to the NF functionality should contain a phase-gradient term $\vec{\zeta} \cdot \vec{r}$ (with $\left| \vec{\zeta} \right|$ larger than the vacuum vector $\left| \vec{k}_0 \right|$) to facilitate the conversion from incident PW to SW. Follow this strategy, we design and fabricate three different meta-devices and experimentally characterize their bi-channel wave-control functionalities. Our experiments illustrate that the first two devices multiplex NF and FF optical-vortex generations with different topological charges while the third one can realize anomalous surface

plasmon polariton (SPP) focusing in the NF and hologram formation in the FF, under excitation of light with left-circular-polarization (LCP) and right-circular-polarization (RCP), respectively. Experimental measurements are in excellent agreement with theoretical predictions.

Results and discussion

Design strategy and characterizations of meta-atoms

Similar to other bi-functional metasurfaces, the presently designed bi-channel metasurface should also exhibit two different phase profiles $\Phi_{NF}(\overrightarrow{r})$ and $\Phi_{FF}(\overrightarrow{r})$, dictated by the pre-designed NF and FF wave-control functionalities, as shined by CP light with opposite helicities. An essential difference here is that $\Phi_{NF}(\overrightarrow{r})$ must contain a phase gradient term to help convert PW to SW while $\Phi_{FF}(\overrightarrow{r})$ does not need such a term. Without losing generality, we assume that the NF and FF functionalities correspond to LCP and RCP incidences, respectively. Therefore, once the bi-channel metasurface is shined by a linearly polarized (LP) light, both a FF beam and a NF wave pattern can be generated simultaneously, without mutual interferences as they are in different channels by nature. To design such a bi-channel metasurface, we firstly need to find a set of meta-atoms exhibiting independently tuned reflection phases under LCP and RCP incidences.

We find that meta-atoms in metal/insulator/metal (MIM) configuration are appropriate building blocks to construct our bi-channel metasurfaces. As schematically shown in the inset to Fig. 1, an MIM meta-atom consists of a metallic resonator with anisotropic shape and a continuous metal film separated by a dielectric spacer. We assume that the meta-atom exhibits mirror reflection symmetries on the *xoy* plane with two principle
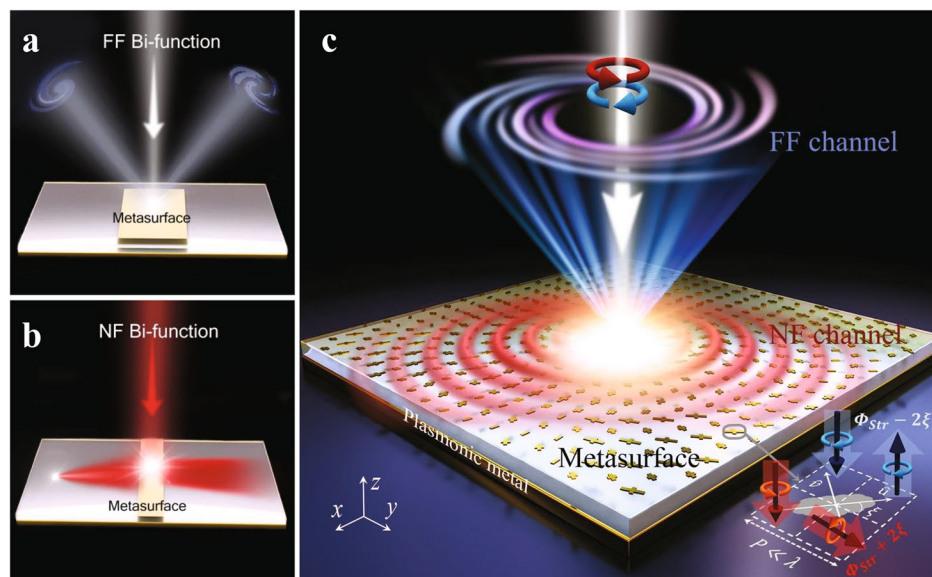
Fig. 1 Working principle of the bi-channel meta-surface. Schematics of **a** a FF bi-functional meta-device and **b** a NF bi-functional meta-device realized previously, and schematics of **c** the bi-channel meta-device proposed in this article which exhibit distinct pre-designed wave-control functionalities in NF and FF channels, respectively, under excitations of circularly polarized light with opposite helicities. The constitutional meta-atoms are in metal/insulator/metal configuration with top metallic resonators possessing tailored anisotropy and being rotated by an angle *ξ* with respect to the laboratory frame (inset at the right-hand side)

axes denoted $\hat{u}$ and $\hat{v}$, and is rotated by an angle of ξ around the z axis. Let r_{uu} and r_{vv} denote, respectively, the reflection coefficients of the meta-atom under illuminations of LP light polarized along two principles axes, we find that the Jones Matrix of the rotated MIM meta-atom in the CP bases is $\widetilde{\mathbf{R}} = \mathbf{S}\mathbf{M}(\xi)\begin{pmatrix} r_{uu} & \\ & r_{vv} \end{pmatrix}\mathbf{M}(\xi)^{-1}\mathbf{S}^{-1}$, where $\mathbf{M}(\xi) = \begin{pmatrix} \cos\xi & -\sin\xi \\ \sin\xi & \cos\xi \end{pmatrix}$ and $\mathbf{S} = \frac{\sqrt{2}}{2}\begin{pmatrix} 1 & -i \\ 1 & i \end{pmatrix}$ describe, respectively, the rotation operation and the LP to CP transformation. Simple calculations show that

$$\widetilde{\mathbf{R}}|\sigma\rangle_{\text{in}} = \left(\frac{r_{uu} + r_{vv}}{2}\right)|\sigma\rangle_{\text{ref}} + \left(\frac{r_{uu} - r_{vv}}{2}\right)e^{i\sigma 2\xi}|-\sigma\rangle_{\text{ref}} \tag{1}$$

with $|\sigma\rangle = |+\rangle$ and $|\sigma\rangle = |-\rangle$ denoting the LCP and RCP states at the incident side, respectively. Equation (1) indicates that, shining the meta-atom by incident CP light with a particular spin, the reflected wave generally contains two parts –- a spin-maintained normal mode with the coefficient $(r_{uu} + r_{vv})/2$ and an anomalous mode with the coefficient $(r_{uu} - r_{vv})e^{i\sigma 2\xi}/2$ carrying a spin-dependent phase $\sigma \cdot 2\xi = \sigma \cdot \Phi_{\text{PB}}$ of a PB origin. To avoid interferences of the normal mode without desired PB phases, we assume that all meta-atoms behave as ideal half-wave-plates (HWPs) with zero normal mode strength,

$$A_n = \frac{|r_{uu} + r_{vv}|}{2} = 0. \tag{2}$$

Under such condition, Eq. 1 is simplified as

$$\widetilde{\mathbf{R}}|\sigma\rangle_{\text{in}} = \left(\frac{r_{uu} - r_{vv}}{2}\right)e^{i\sigma 2\xi}|-\sigma\rangle_{\text{ref}} = A_a e^{i(\Phi_{\text{Str}} + \sigma \cdot \Phi_{\text{PB}})}|-\sigma\rangle_{\text{ref}} \tag{3}$$

with $\Phi_{\text{Str}} = \arg(r_{uu} - r_{vv})$ being the structural phase dictated by local resonances and $A_a = |r_{uu} - r_{vv}|/2$ being the strength of anomalous mode. Clearly, now such an MIM meta-atom exhibits delinked reflection properties under excitations of CP light with different helicities. Therefore, constructing a metasurface with a series of meta-atoms satisfying Eq. (2) but exhibiting different structures and orientation angles (and thus different Φ_{Str} and Φ_{PB}), the device must exhibit two different phase distributions

$$\begin{cases} \Phi_{\text{NF}}\left(\overrightarrow{r}\right) = \Phi_{\text{Str}}\left(\overrightarrow{r}\right) + 2\xi\left(\overrightarrow{r}\right) \\ \Phi_{\text{FF}}\left(\overrightarrow{r}\right) = \Phi_{\text{Str}}\left(\overrightarrow{r}\right) - 2\xi\left(\overrightarrow{r}\right) \end{cases} \tag{4}$$

for LCP and RCP incidences, respectively. Thus, with $\Phi_{\text{NF}}\left(\overrightarrow{r}\right)$ and $\Phi_{\text{FF}}\left(\overrightarrow{r}\right)$ known for two target wave-control functionalities in NF and FF regions, we can retrieve the corresponding distributions of structural and PB phases:

$$\begin{cases} \Phi_{\text{Str}}\left(\overrightarrow{r}\right) = \frac{\Phi_{\text{NF}}\left(\overrightarrow{r}\right) + \Phi_{\text{FF}}\left(\overrightarrow{r}\right)}{2} \\ \xi\left(\overrightarrow{r}\right) = \frac{\Phi_{\text{NF}}\left(\overrightarrow{r}\right) - \Phi_{\text{FF}}\left(\overrightarrow{r}\right)}{4} \end{cases}, \tag{5}$$

from which we can further determinate the structural parameters and orientation angles of constitutional meta-atoms at different positions.
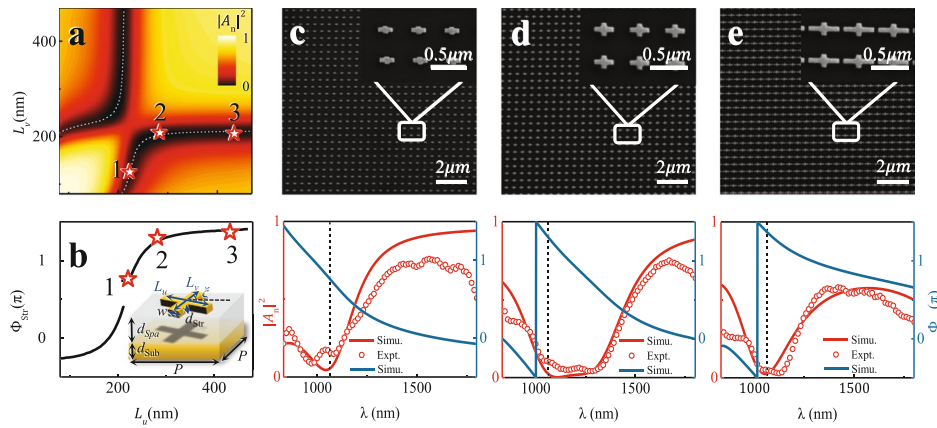
Fig. 2 Meta-atom design strategy and characterizations of three typical meta-atoms. **a** Simulated normal-mode intensity $|A_n|^2$ of the MIM meta-atom against their bar lengths L_u and L_v, with the dashed curve marking Min($|A_n|^2$) for each L_u. **b** Simulated structural phase Φ_{Str} of the MIM meta-atom as a function of the bar length L_u with L_v taking the values on the Min($|A_n|^2$) curve in **a** correspondingly. Inset in **b** illustrates the basic structure of an MIM meta-atom. Three stars labelled as "1, 2, 3" correspond to three stars in **a**. **c**, **d**, **e** Upper panels are SEM pictures of three meta-atoms labelled as "1, 2, 3" in **a** and **b**, respectively; Lower panels depict the $|A_n|^2$ spectra obtained by simulations (red line) and measurements (red circle) and the simulated spectra of Φ_{Str} (blue line) for three meta-atoms denoted "1, 2, 3" in **a** and **b**. Dashed lines in these figures indicate the positions of working wavelength ($\lambda = 1064$ nm)

We now design a series of meta-atoms suitable for construction of our bi-channel metasurfaces and experimentally characterize their optical properties. As shown in the inset to Fig. 2b, the top-layer resonator is an anisotropic Au cross formed by two bars with lengths L_u and L_v, and the spacer is a silicon dioxide (SiO$_2$) layer. The spacer thickness and the bar width are fixed as $D_{Spa} = 100nm$, $w = 80nm$, while the periodicity of the meta-atom array is set as $P = 480nm$. To guide the generated SWs out of the metasurface, we include a plasmonic metal supporting eigen SPP adjacent to the metasurface. To minimize the scatterings at the boundary, such plasmonic metal is chosen as a 50 nm-thick layer of Au covered by a 100 nm-thick SiO2 layer, being exactly the same structure as the MIM structure with top resonator removed. In addition, the phase gradient $\left|\vec{\zeta}\right|$ adopted in $\Phi_{NF}(\vec{r})$ should match the SPP wave-vector k_{SPP} of the plasmonic metal. Numerical simulations show that $k_{SPP} = 1.108k_0$ at the wavelength of 1064 nm (see Sec. 1 in SI).

We now illustrate how to determine the structural parameters of our MIM meta-atoms. Previous studies[56] have shown that the reflection coefficient $r_{uu} = |r_{uu}|e^{i\Phi_{uu}}$ ($r_{vv} = |r_{vv}|e^{i\Phi_{vv}}$) of an MIM meta-atom can be strongly modulated as frequency passes through a magnetic-resonance frequency f_{uu} (f_{vv}), dictated mainly by the structural parameter L_u (L_v) with other geometric parameters fixed. Therefore, fix the working wavelength at 1064 nm, we find that varying two structural parameters L_u and L_v can effectively modulate the two magnetic-resonance frequencies, which in turn, tune the values of r_{uu} and r_{vv} (see Fig. S2 in SI for corresponding phase diagrams). Fig. 2a depicts how the normal-mode strength $|A_n|^2$ varies against L_u and L_v, calculated at the wavelength of 1064 nm. Clearly, two minimum-$|A_n|^2$ lines in the phase diagram indicate proper candidates satisfying Eq. (2). Meanwhile, Fig. 2b demonstrates the corresponding structural phase for the points on the line, again calculated at the

wavelength of 1064 nm. Based on the results shown in Fig. 2b, we successfully select a series of meta-atoms with Φ_{Str} covering a large variation range, yet all exhibiting minimum values of $|A_{\mathrm{n}}|^2$ suitable for building our meta-devices.

Three representative points lying on the Min($|A_{\mathrm{n}}|^2$)-curve denoted by open stars in Fig. 2a and b are selected for experimental illustration of typical meta-atoms (see Sec.3.1 of SI for geometric parameters). We fabricate three metasurfaces using standard electron-beam lithography (EBL) technology (see Materials and methods for fabrication details), each consisting of a periodic array for one meta-atom specified in Fig. 2a, with their scanning-electron-microscopy (SEM) pictures shown in upper panels of Fig. 2c-e. With these samples at hand, we then measure their co-polarization reflection spectra as the metasurfaces are shined by normally incident LP light with **E** field polarized at an angle 45° in-between *u* and *v* axes (see Sec.3.2 in SI for calculated reflection spectra of the three samples). We note that the measured $|A_{\mathrm{n}}|^2$ can be easily retrieved from raw experimental data (see more details in Sec. 3.3 of the SI), and the lower panels of Fig. 2c-e depict the measured $|A_{\mathrm{n}}|^2$ spectra of three samples, compared with corresponding simulation results. Simulations are in nice agreement with the measured $|A_{\mathrm{n}}|^2$ spectra, both showing that $|A_{\mathrm{n}}|^2 \approx 0$ at 1064 nm for all meta-atoms, indicating that they are appropriate building blocks satisfying Eq. (2). Unfortunately, we do not have the experimental facility to directly measure Φ_{Str} of these meta-atoms, thus only numerical simulations are shown in Fig. 2b-e. Though only three typical examples are demonstrated experimentally here, meta-atoms with varied structural parameters covering the whole structural phase line (a nearly 2π range) shown in Fig. 2b are employed in realistic designs of our functional devices. Employing both spin-independent structural phase covering a nearly 2π range and spin-dependent PB phase freely tunable by rotation of structures, delinked functionalities in NF and FF channels can be easily realized by our proposed meta-devices. With such a meta-atom database set up, we can design any bi-channel metasurfaces by selecting a series of meta-atoms with the $\{\Phi_{\mathrm{Str}}(\overrightarrow{r}), \xi(\overrightarrow{r})\}$ distribution solved from Eq. (5).

Bi-channel meta-devices I & II: multiplexing NF & FF vortex generations

As an illustration of our proposed strategy, we first design and realize two meta-devices that, can generate a vortex SPP and a spatial vortex beam with different topological charges under illumination of LCP and RCP light. According to the target NF and FF functionalities, we expect that our meta-device should exhibit the following phase distributions

$$\Phi_{\mathrm{NF}}(\overrightarrow{r}) = -\zeta_r r + l_{\mathrm{NF}}\varphi; \; \Phi_{\mathrm{FF}}(\overrightarrow{r}) = l_{\mathrm{FF}}\varphi - \frac{\pi}{2} \tag{6}$$

under LCP and RCP incidences (for NF and FF channels) respectively. Here, (r, φ) denotes a position in the local polar system; $\zeta_r = 1.108k_0$ is the radial phase gradient that can couple the LCP component of the incident light to a cylindrically polarized SPP flowing to the origin point on the metallic surface; l_{NF} and l_{FF} are topological charges possessed by waves generated in NF and FF channels, respectively. We can then retrieve the $\{\Phi_{\mathrm{Str}}(\overrightarrow{r}), \xi(\overrightarrow{r})\}$ distributions from Eq. (6),

$$\Phi_{\mathrm{Str}}(\overrightarrow{r}) = \frac{-\zeta_r r + l_{\mathrm{NF}}\varphi + l_{\mathrm{FF}}\varphi}{2} - \frac{\pi}{4}; \; \xi(\overrightarrow{r}) = \frac{-\zeta_r r + l_{\mathrm{NF}}\varphi - l_{\mathrm{FF}}\varphi}{4} + \frac{\pi}{8}, \qquad (7)$$

which, in turn, help us determine the structural parameters (L_u, L_v) and orientation angle of a meta-atom located at the position $\overrightarrow{r}$, based on the strategy described in last sub-section.

As the first example, we design and fabricate a meta-device with $l_{\mathrm{NF}} = +1$ and $l_{\mathrm{FF}} = -3$. Following the strategy described above, we put $l_{\mathrm{NF}} = +1$ and $l_{\mathrm{FF}} = -3$ into Eq. (7) to get the $\{\Phi_{\mathrm{Str}}(\overrightarrow{r}), \xi(\overrightarrow{r})\}$ distributions and then depict them in Fig. 3b and c, respectively. Based on these two distributions, we successfully retrieve the bar lengths $\{L_u, L_v\}$ (see Fig. 3d and e) and orientation angles (see Fig. 3c) of meta-toms at different positions, and finally fabricate the sample using standard EBL technology. Figure 3f depicts the SEM picture of the whole sample, while Fig. 3g contains a zoomed-in picture of the centre framed area in Fig. 3f.

Shine the metasurface by normally incident CP light beams with different helicities at $\lambda = 1064$ nm, we experimentally characterize the bi-channel wave-manipulation
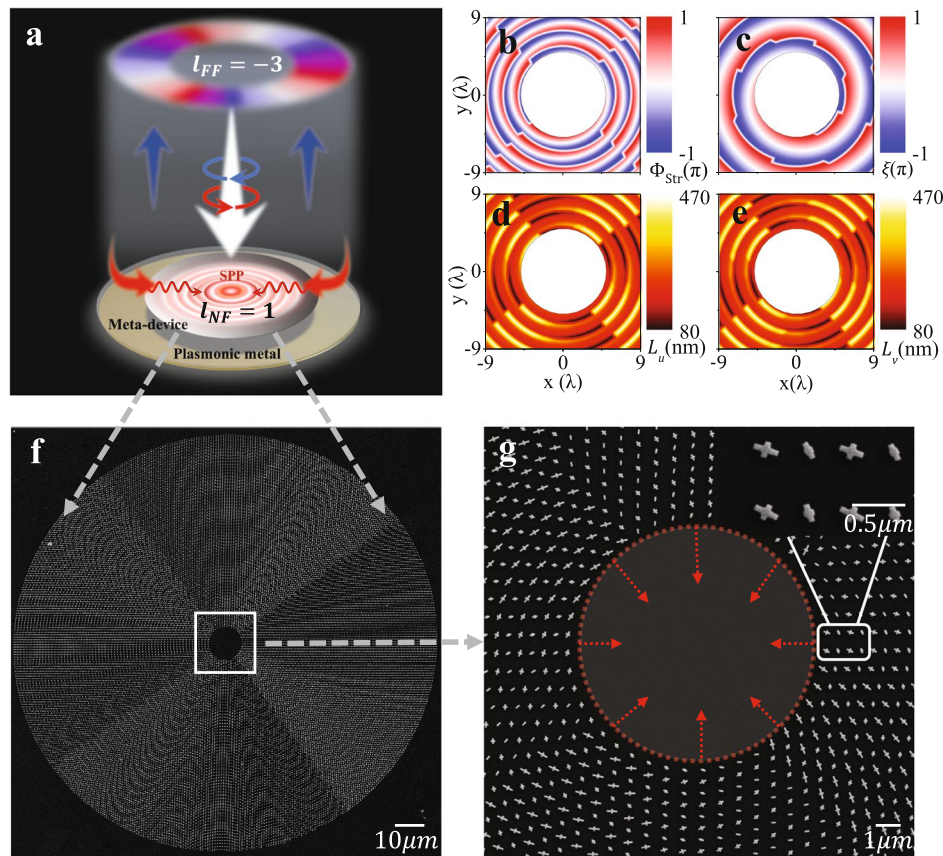
Fig. 3 Expected functionality, structural parameters and sample pictures of the meta-device I. **a** The proposed meta-device I is expected to covert the incident LCP light to a focused vortex SPP in the NF channel and reflect the incident RCP light to a spatial vortex beam in the FF channel, with topological charges of two vertices being 1 and -3, respectively. Distributions of **b** $\Phi_{\mathrm{Str}}(\overrightarrow{r})$, **c** $\xi(\overrightarrow{r})$, **d** $L_u(\overrightarrow{r})$ and **e** $L_v(\overrightarrow{r})$ of the meta-device under design. **f** SEM image of the fabricated sample, with its zoomed-in images shown in **g** and the inset
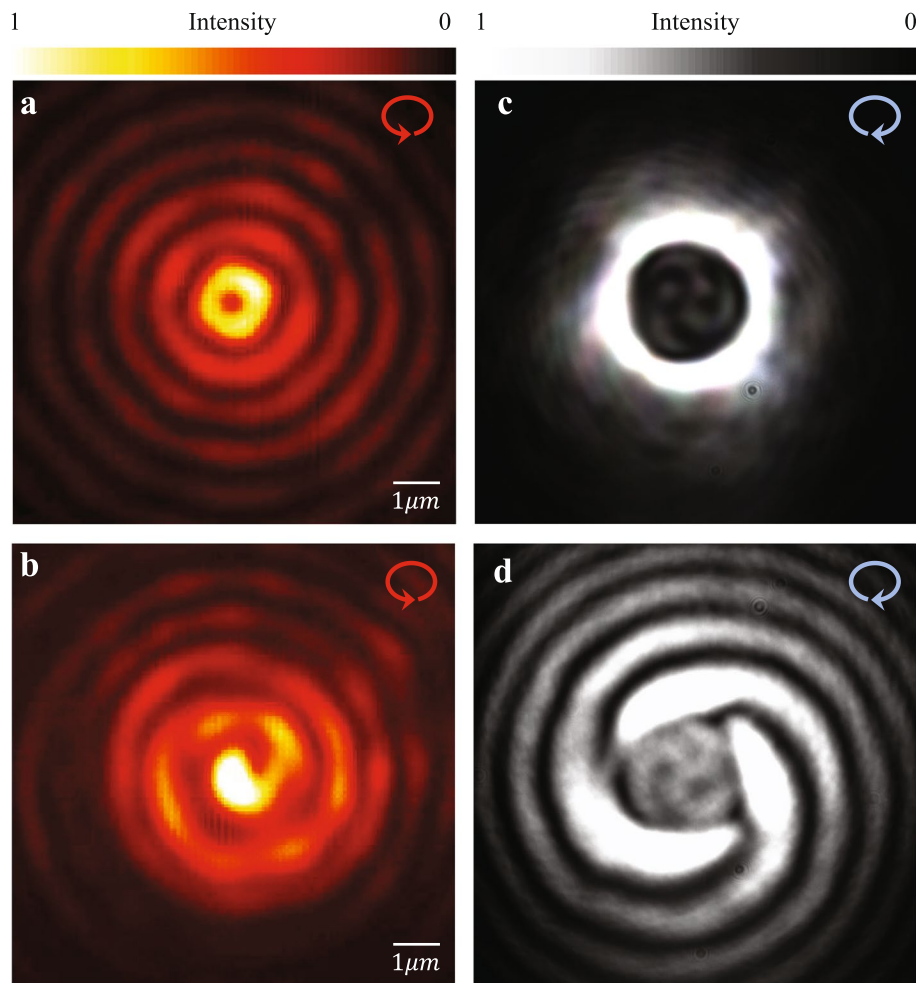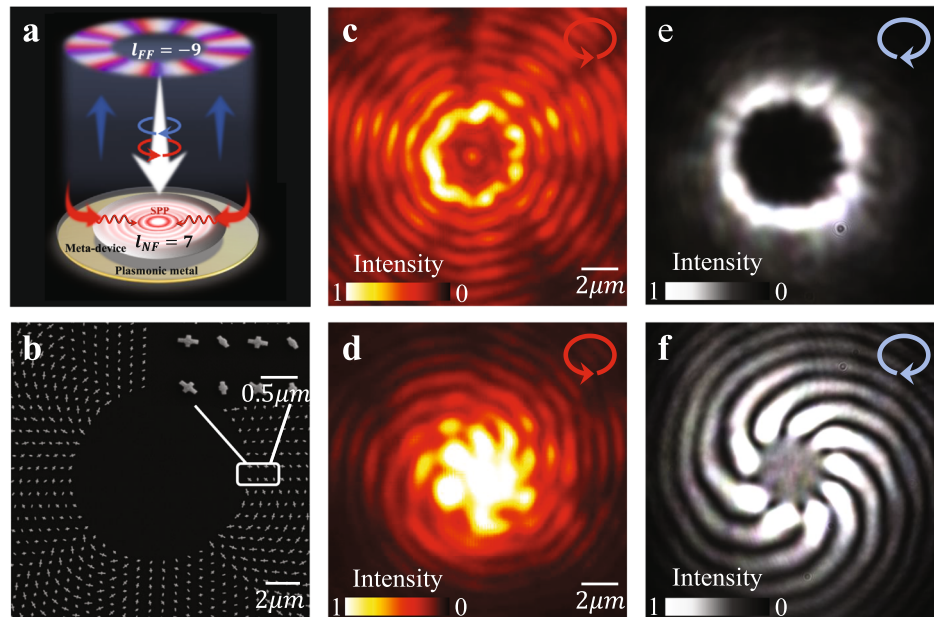
Fig. 4 Experimental characterizations of the bi-channel meta-device I. As shined by LCP light at 1064 nm, **a** the LRM-recorded field pattern of the vortex SPP generated on the sample surface and **b** the CCD-captured field pattern as the vortex SPP interferes with a spherical wave. As shined by RCP light at 1064 nm, **c** the CCD-captured field pattern of the vortex beam reflected by the device and **d** the CCD-captured field pattern as the vortex beam interferes with a spherical wave

capability of the fabricated device. Consider the LCP incidence first where a vortex SPP is expected to be generated in the central region of the device. We utilize a home-made leakage radiation microscopy (LRM) to record the NF pattern generated on the device surface (see Fig. S10 in SI for experimental setup of the LRM system). From Fig. 4a where the LRM-recorded NF-pattern is depicted, we see clearly that the generated NF is an SPP beam focused to the origin point. The existence of a zero-field singularity in the centre already implies that the generated SPP beam carries an orbital angular momentum (OAM). Interfering the generated NF SPP with a spherical wave using a homemade Michelson interferometer, we find that the interference yields a clear 1st-order anti-clockwise spiral pattern (see Fig. 4b), indicating that the generated NF SPP is a vortex carrying a topological charge $l_{\text{NF}} = +1$. As the incident polarization changes to RCP, the charge-coupled device (CCD)-captured image

of the reflected wave in the FF exhibits a clear donut shape (Fig. 4c), implying that the FF beam also carries an OAM. Figure 4d depicts the pattern formed by interfering the generated FF beam with a spherical beam. The 3rd-order clockwise spiral shape proves that the topological charge carried by the FF beam is $l_{FF} = -3$. Interference results with quasi-plane waves are also presented in Fig. S4 of SI, further proving the generation of OAMs with independent topological charges in NF and FF respectively.

Our proposed strategy is so general that it can also be employed to realize other bi-channel meta-devices exhibiting larger topological charges (Fig. 5a). Taking{$l_{NF} = +7$,$l_{FF} = -9$} as an example, we follow the same procedure as in last section to design and fabricate a meta-device (see distributions of geometric parameters in Sec.5.1 of SI and Fig. 5b for SEM image), and then utilize the same experimental setup to characterize the properties of beams generated in the NF and FF, respectively. Shine the meta-device by LCP light at 1064 nm, we use the LRM system to record the NF-channel field distribution generated on the device (Fig. 5c). The generated NF pattern shows clear features of a focused SPP carrying an OAM: 1) the field intensity grows as approaching the origin point; 2) a zero-field hole appears in the middle of the 2D focused SPP. Changing the incident polarization from LCP to RCP, we find that the reflected beam becomes a vortex beam propagating to the FF, as shown in the CCD-recorded image in Fig. 5e. Performing the same interference experiments with a reference spherical wave in both NF and FF channels, we obtain interference patterns

Fig. 5 Expected functionality, sample picture, and experimental characterization of the bi-channel meta-device II. **a** The proposed meta-device II is expected to covert the incident LCP light to a focused vortex SPP in the NF channel and reflect the incident RCP light to a spatial vortex beam in the FF channel, with vertices' topological charges being 7 and -9, respectively. **b** SEM image of the fabricated sample, with its zoomed-in images shown in the inset. As the meta-device is shined by LCP light at 1064 nm, **c** the LRM-recorded field pattern of the vortex SPP generated on the metallic surface and **d** the CCD-captured field pattern as the vortex SPP interferes with a spherical wave. As the meta-device is shined by RCP light at 1064 nm, **e** the CCD-captured field pattern of the vortex beam reflected by the device and **f** the CCD-captured field pattern as the vortex beam interferes with a spherical wave

(Figs. 5d and f) revealing clearly that $l_{\mathrm{NF}} = +7$ and $l_{\mathrm{FF}} = -9$, respectively. Additional experimental results concerning interferences with quasi-plane waves can be found in Fig. S6 of SI.

Bi-channel meta-device III: multiplexing NF SPP anomalous focusing and FF hologram

The proposed scheme is not limited to the realizations of bi-channel meta-devices exhibiting similar functionalities, but generic enough to design bi-channel meta-devices exhibiting distinct functionalities in two channels. As an explicit illustration, we further realize a meta-device that can generate an anomalously focused SPP beam and a pre-designed hologram in the NF and FF channels, under excitations of LCP and RCP light at 1064 nm, respectively. According to the theory presented in last section, we expect our meta-device to exhibit the following phase distributions:

$$
\begin{aligned}
\Phi_{\mathrm{NF}}(\overrightarrow{r}) &= k_{\mathrm{SPP}}x - k_{\mathrm{SPP}}\left(\sqrt{(y-F_y)^2 + F_x^2} - F_x\right) \\
\Phi_{\mathrm{FF}}(\overrightarrow{r}) &= \Phi_{\mathrm{Diag}}(\overrightarrow{r})
\end{aligned}
\tag{8}
$$

for the NF and FF channels, respectively. Here, $k_{\mathrm{SPP}} > k_0$ and thus the term $k_{\mathrm{SPP}}x$ can couple the incident LCP light to a unidirectional SPP, while the second term in Φ_{NF} can help focus the generated SPP beam onto a point with focal length $F = \sqrt{F_x^2 + F_y^2}$ at an angle θ determined by $\theta = \tan^{-1}(\frac{F_y}{F_x})$, and $\Phi_{\mathrm{Diag}}(\overrightarrow{r})$ is the phase distribution retrieved from the target FF hologram by the Gerchberg-Saxton (GS) algorithm[57].

Substituting Eq. (8) into Eq. (5), we retrieve the $\{\Phi_{\mathrm{Str}}(\overrightarrow{r}), \xi(\overrightarrow{r})\}$ distributions as:

$$
\begin{aligned}
\Phi_{\mathrm{str}}(\overrightarrow{r}) &= \frac{k_{\mathrm{SPP}}x - k_{\mathrm{SPP}}\left(\sqrt{(y-F_y)^2 + F_x^2} - F_x\right) + \Phi_{\mathrm{Diag}}(\overrightarrow{r})}{2} \\
\xi(\overrightarrow{r}) &= \frac{k_{\mathrm{SPP}}x - k_{\mathrm{SPP}}\left(\sqrt{(y-F_y)^2 + F_x^2} - F_x\right) - \Phi_{\mathrm{Diag}}(\overrightarrow{r})}{4}
\end{aligned},
\tag{9}
$$

which help us sort out all needed meta-atoms from the database that we have built. We then finish the design and fabricate the sample using standard EBL technology, with the SEM picture of our sample depicted in Fig. 6b (see distributions of geometric parameters in Sec.6.2 of SI). We note that the sample exhibits a rectangular shape in accordance with its designed NF functionality.

We experimentally characterize the bi-channel functionalities of the fabricated meta-device. Shine the sample by normally incident LCP and RCP light at 1064 nm, we employ the LRM system and a micro-imaging system (for far-field hologram characterization) to capture the field patterns generated in the NF and FF channels (see Fig. S11 in SI for the far-field experimental setup), respectively. As shown in Fig. 6c, an SPP beam is generated on the metal surface at the right-hand side of the sample, which is then anomalously deflected to an angle of 30° with respect to the x axis and subsequently focused to a focal point 15 μm away from the sample edge. All these results are well-consistent with our theoretical predictions. Meanwhile, Fig. 6d depicts the hologram image captured by our CCD in the FF, containing well-recognized English symbols "C", "H" as well "ZHOU GROUP". Again, the generated image is consistent with the pre-designed pattern (see Fig. S7 in SI).
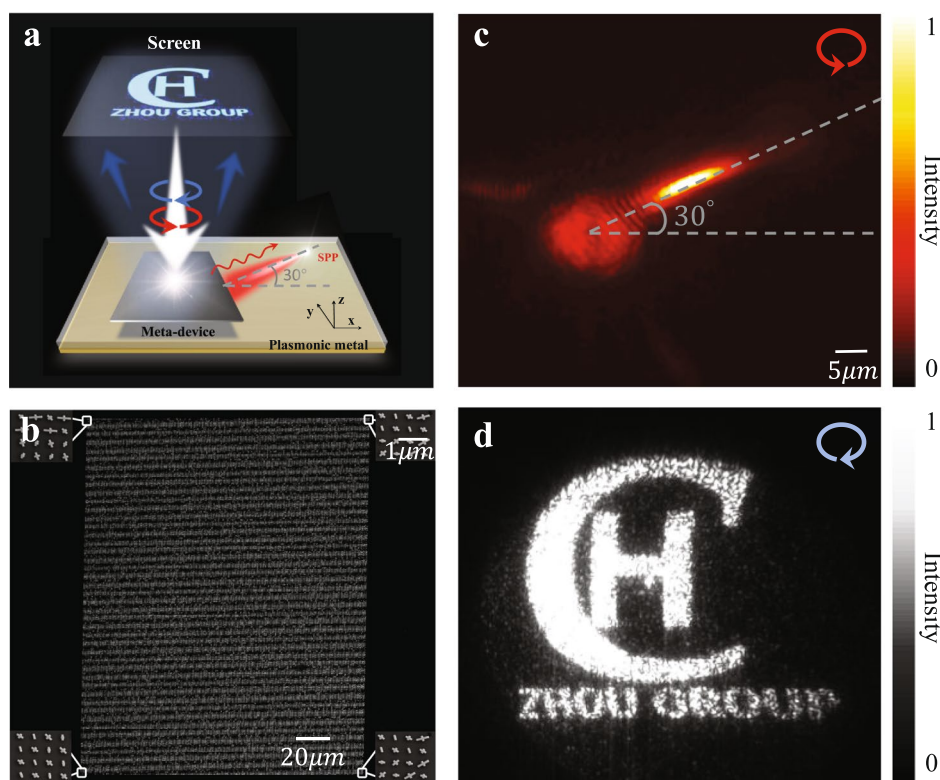
Fig. 6 Expected functionality, sample picture, and experimental characterizations of the bi-channel meta-device III. **a** The proposed meta-device III is expected to covert the incident LCP light to an anomalously focused NF SPP beam and generate a pre-designed FF hologram as the device is shined by an RCP light. **b** SEM image of the fabricated sample. **c** The LRM-recorded near-field pattern generated on the metallic surface, representing an anomalously deflected SPP beam which is then focused to a pre-designed focal point, as the meta-device is shined by LCP light at 1064 nm. **d** The CCD-captured hologram image in the far field as the meta-device is shined by RCP light at 1064 nm

Conclusions

In short, we propose a generic strategy to realize meta-devices that can multiplex wave-manipulation capabilities in two spatially non-overlapping channels (i.e., NF and FF channels), employing meta-atoms exhibiting arbitrary spin-delinked reflection phases dictated by both resonant and PB mechanisms. We employ the proposed scheme to design/fabricate three meta-devices and then experimentally demonstrate their bi-channel wave-manipulation functionalities. Specifically, the first two meta-devices can multiplex vortex-beam generations with different topological charges in the NF and FF channels, while the third one can generate a hologram in the FF channel and an anomalously deflected focusing SPP beam in the NF channel. Due to difficulties in experiments, we employ numerical simulations to evaluate the efficiencies of our meta-devices together with several previously realized meta-devices with similar bi-functionalities. Comparisons shown in Sec. 7 of SI reveal that our devices exhibit higher working efficiencies than previously designed meta-devices. Although we only realized bi-channel meta-devices in this manuscript, there are many possible ways to increase the functionality channel of the meta-device. For example, adopting

meta-atoms *not* exhibiting perfect polarization conversion capabilities to construct our meta-device, we can purposely encode a desired phase distribution to the normal mode generated by the meta-device as shined by CP light; employing *angular-dispersive* meta-atoms, we can precisely design different phase distributions at the incidence of varied angles. Through these methods to increase degrees of freedom involved in the meta-system, we can finally expand functionality channel quantities for the realized meta-device. Our results open up a new avenue for achieving multi-functional optical devices working in non-overlapping spaces without mutual interferences, which may stimulate many follow-up research works (e.g., extending to transmission geometry and arbitrary incident polarizations) and inspire useful applications in integration optics.

Methods

Numerical simulation

In our finite-difference time-domain simulations, the permittivity of Au is described by the Drude model $\varepsilon_r(\omega) = \varepsilon_\infty - \frac{\omega_p^2}{\omega(\omega + i\gamma)}$, with $\varepsilon_\infty = 9, \omega_p = 1.367 \times 10^{16} s^{-1}, \gamma = 2.448 \times 10^{14} s^{-1}$, obtained by fitting with experimental results. The SiO$_2$ spacer is considered as a lossless dielectric with permittivity $\varepsilon = 2.25$. Additional losses caused by surface roughness and grain boundary effects in thin films as well as dielectric losses are effectively considered in the fitting parameter γ.

Sample fabrications

All MIM samples are fabricated using standard thin-film deposition and EBL techniques. In the first step, we sequentially deposite 5 nm – thick Cr, 50 nm – thick Au, 5 nm Cr and a 100 nm—thick SiO$_2$ dielectric layer onto a silicon substrate using magnetron DC sputtering (Cr and Au) and RF sputtering (SiO$_2$). Then, we lithograph the cross structures with EBL, employing an ~ 100 nm thick PMMA2 layer at an acceleration voltage of 20 keV. After development in a solution of methyl isobutyl ketone and isopropyl alcohol, a 5 nm Cr adhesion layer and a 30 nm Au layer are subsequently deposited using thermal evaporation. The Au patterns are finally formed on top of the SiO$_2$ film after a lift-off process using acetone.

Experimental setup

We use a near-infrared (NIR) microimaging system to characterize the performance of all designed meta-atoms. A broadband supercontinuum laser (Fianium SC400) source and a fibre-coupled grating spectrometer (Ideaoptics NIR2500) are used in the FF measurements. A beam splitter, a linear polarizer and a CCD are also used to measure the reflectance and analyse the polarization distributions.

An NIR microimaging system with a homemade Michelson interferometer is employed to perform real-time imaging of the FF component and its interferences with the reference light. As for the NF characterization, a typical LRM system combined with a Michelson-type interferometer is employed for real-time imaging of the excited SPP and its interference with the reference light.

Abbreviations

PW   Propagating wave
SW   Surface wave
FF   Far-field
NF   Near-field
PB   Pancharatnam — Berry
SPP   Surface plasmon polariton
LCP   Left-circular-polarization
RCP   Right-circular-polarization
LP   Linearly polarized
MIM   Metal/insulator/metal
HWPs   Half-wave-plates
SiO2   Silicon dioxide
EBL   Electron-beam lithography
SEM   Scanning-electron-microscopy
LRM   Leakage radiation microscopy
OAM   Orbital angular momentum
CCD   Charge-coupled device

Supplementary Information

The online version contains supplementary material available at https://doi.org/10.1186/s43074-024-00128-5.

> **Supplementary Material 1.**

Availability of data and materials

The datasets used and/or analyzed during the current study are available from the corresponding author on reasonable request.

Declarations

Ethics approval and consent to participate

Not applicable.

Consent for publication

Not applicable.

Competing interests

The authors declare that they have no competing interests.

References

1. Zhang JJ, Xiao SS, Wubs M, Mortensen NA. Surface plasmon wave adapter designed with transformation optics. ACS Nano. 2011;5:4359–64.
2. Sun SL, He Q, Xiao SY, Xu Q, Li X, Zhou L. Gradient-index meta-surfaces as a bridge linking propagating waves and surface waves. Nat Mater. 2012;11:426–31.
3. Xu Q, Lang Y, Jiang X, Yuan X, Xu Y, Gu J, et al. Meta-optics inspired surface plasmon devices. Photonics Insights. 2023;29(1):R02.
4. Zhao M, Zhou Y, Li X, Cao W, He C, Yu B, et al. Applications of satellite remote sensing of nighttime light observations: advances, challenges, and perspectives. Remote Sens. 2019;11(17):1971.

5. Ma Q, Liu C, Xiao Q, Gu Z, Gao X, Li L, et al. Information metasurfaces and intelligent metasurfaces. Photonics Insights. 2022;1(1):R01.

6. Richardson DJ, Fini JM, Nelson LE. Space-division multiplexing in optical fibres. Nat Photonics. 2013;7:354–62.

7. Khalighi MA, Uysal M. Survey on free space optical communication: a communication theory perspective. IEEE Communications Surveys & Tutorials. 2014;16:2231–58.

8. Wang J. Advances in communications using optical vortices. Photonics Research. 2016;4(5):B14-28.

9. Jia Q, Lyu W, Yan W, Tang W, Lu J, Qiu M. Optical manipulation: from fluid to solid domains. Photonics Insights. 2023;2(2):R05.

10 Li T, Chen C, Xiao X, Chen J, Hu S, Zhu S. Revolutionary meta-imaging: from superlens to metalens. Photonics Insights. 2023;2(1):R01.

11. Fang N, Lee H, Sun C, Zhang X. Sub-diffraction-limited optical imaging with a silver superlens. Science. 2005;308:534–7.

12. Wei F, Lu D, Shen H, Wan W, Ponsetto JL, Huang E, et al. Wide field super-resolution surface imaging through plasmonic structured illumination microscopy. Nano Lett. 2014;14:4634–9.

13. Willets KA, Wilson AJ, Sundaresan V, Joshi PB. Super-resolution imaging and plasmonics. Chem Rev. 2017;117:7538–82.

14. Anker JN, Hall WP, Lyandres O, Shah NC, Zhao J, Van Duyne RP. Biosensing with plasmonic nanosensors. Nat Mater. 2008;7:442–53.

15. Zhang S, Bao K, Halas NJ, Xu H, Nordlander P. Substrate-induced Fano resonances of a plasmonic nanocube: a route to increased-sensitivity localized surface plasmon resonance sensors revealed. Nano Lett. 2011;11:1657–63.

16. Zhao Y, Tong RJ, Xia F, Peng Y. Current status of optical fiber biosensor based on surface plasmon resonance. Biosens Bioelectron. 2019;142: 111505.

17 Yao J, Ou J-Y, Savinov V, Chen MK, Kuo HY, Zheludev NI, et al. Plasmonic anapole metamaterial for refractive index sensing. PhotoniX. 2022;3(1):23.

18. Citrin DS. Coherent excitation transport in metal-nanoparticle chains. Nano Lett. 2004;4:1561–5.

19. Fedotov VA, Rose M, Prosvirnin SL, Papasimakis N, Zheludev NI. Sharp trapped-mode resonances in planar metamaterials with a broken structural symmetry. Phys Rev Lett. 2007;99: 147401.

20. Yin Y, Qiu T, Li J, Chu PK. Plasmonic nano-lasers. Nano Energy. 2012;1:25–41.

21. Hao JM, Yuan Y, Ran LX, Jiang T, Kong JA, Chan CT, et al. Manipulating electromagnetic wave polarizations by anisotropic metamaterials. Phys Rev Lett. 2007;99(6):063908.

22 Hao JM, Ren QJ, An ZH, Huang XQ, Chen ZH, Qiu M, et al. Optical metamaterial for polarization control. Phys Rev A. 2009;2:023807.

23. Pors A, Nielsen MG, Della Valle G, Willatzen M, Albrektsen O, Bozhevolnyi SI. Plasmonic metamaterial wave retarders in reflection by orthogonally oriented detuned electrical dipoles. Opt Lett. 2011;36:1626–8.

24. Sun WJ, He QO, Hao JM, Zhou L. A transparent metamaterial to manipulate electromagnetic wave polarizations. Opt Lett. 2011;36:927–9.

25. Yu NF, Aieta F, Genevet P, Kats MA, Gaburro Z, Capasso F. A broadband, background-free quarter-wave plate based on plasmonic metasurfaces. Nano Lett. 2012;12:6328–33.

26. Yu NF, Genevet P, Kats MA, Aieta F, Tetienne JP, Capasso F, et al. Light propagation with phase discontinuities: generalized laws of reflection and refraction. Science. 2011;334:333–7.

27. Sun SL, Yang KY, Wang CM, Juan TK, Chen WT, Liao CY, et al. High-efficiency broadband anomalous reflection by gradient meta-surfaces. Nano Lett. 2012;12:6223–9.

28. Ding F, Deshpande R, Meng C, Bozhevolnyi SI. Metasurface-enabled broadband beam splitters integrated with quarter-wave plate functionality. Nanoscale. 2020;12:14106–11.

29. Han W, Yang YF, Cheng W, Zhan QW. Vectorial optical field generator for the creation of arbitrarily complex fields. Opt Express. 2013;21:20692–706.

30. Wang D, Liu F, Liu T, Sun S, He Q, Zhou L. Efficient generation of complex vectorial optical fields with metasurfaces. Light-Sci Appl. 2021;10:67.

31. Liu S, Cui TJ, Noor A, Tao Z, Zhang HC, Bai GD, et al. Negative reflection and negative surface wave conversion from obliquely incident electromagnetic waves. Light-Sci Appl. 2018;7(5):18008.

32 Sun WJ, He Q, Sun SL, Zhou L. High-efficiency surface plasmon meta-couplers: concept and microwave-regime realizations. Light-Sci Appl. 2016;5(1):e16003.

33. Liu Y, Zentgraf T, Bartal G, Zhang X. Transformational plasmon optics. Nano Lett. 2010;10:1991–7.

34. Epstein I, Arie A. Arbitrary bending plasmonic light waves. Phys Rev Lett. 2014;112: 023903.

35. Genevet P, Wintz D, Ambrosio A, She A, Blanchard R, Capasso F. Controlled steering of Cherenkov surface plasmon wakes with a one-dimensional metamaterial. Nat Nanotechnol. 2015;10:804–9.

36. Chen J, Li T, Wang S, Zhu S. Multiplexed holograms by surface plasmon propagation and polarized scattering. Nano Lett. 2017;17:5051–5.

37. Li L, Yao K, Wang Z, Liu Y. Harnessing evanescent waves by bianisotropic metasurfaces. Laser Photonics Rev. 2020;14(12):1900244.

38. Chen WT, Yang KY, Wang CM, Huang YW, Sun G, Chiang ID, et al. High-efficiency broadband meta-hologram with polarization-controlled dual images. Nano Lett. 2014;14:225–30.

39. Pors A, Nielsen MG, Bernardin T, Weeber J-C, Bozhevolnyi SI. Efficient unidirectional polarization-controlled excitation of surface plasmon polaritons. Light-Sci Appl. 2014;3: e197.

40. Huang C, Pan W, Ma X, Luo X. Multi-spectral metasurface for different functional control of reflection waves. Sci Rep. 2016;6:23291.

41. Chen L, Ren T, Zhao Y, Yu Q, Huang Z, Zhang K, et al. Polarization-independent wavefront manipulation of surface plasmons with plasmonic metasurfaces. Adv Opt Mater. 2020;8:2000868.

42. Xiong B, Liu Y, Xu Y, Deng L, Chen C-W, Wang J-N, et al. Breaking the limitation of polarization multiplexing in optical metasurfaces with engineered noise. Science. 2023;379:294–9.

43. Lin J, Mueller JP, Wang Q, Yuan G, Antoniou N, Yuan XC, et al. Polarization-controlled tunable directional coupling of surface plasmon polaritons. Science. 2013;340:331–4.
44. Huang L, Chen X, Bai B, Tan Q, Jin G, Zentgraf T, et al. Helicity dependent directional surface plasmon polariton excitation using a metasurface with interfacial phase discontinuity. Light-Sci Appl. 2013;2: e70.
45. Wen D, Yue F, Li G, Zheng G, Chan K, Chen S, et al. Helicity multiplexed broadband metasurface holograms. Nat Commun. 2015;6:8241.
46   Duan JW, Guo HJ, Dong SH, Cai T, Luo WJ, Liang ZZ, et al. High-efficiency chirality-modulated spoof surface plasmon meta-coupler. Sci Rep. 2017;7(1):1354.
47. Wang D, Liu T, Zhou Y, Zheng X, Sun S, He Q, et al. High-efficiency metadevices for bifunctional generations of vectorial optical fields. Nanophotonics. 2020;10:685–95.
48. Wang Z, Li S, Zhang X, Feng X, Wang Q, Han J, et al. Excite spoof surface plasmons with tailored wavefronts using high-efficiency terahertz Metasurfaces. Adv Sci (Weinh). 2020;7:2000982.
49. Jin R, Tang L, Li J, Wang J, Wang Q, Liu Y, et al. Experimental demonstration of multidimensional and multifunctional metalenses based on photonic spin hall effect. ACS Photonics. 2020;7:512–8.
50   Deng L, Jin R, Xu Y, Liu Y. Structured light generation using angle-multiplexed metasurfaces. Adv Opt Mater. 2023;11(16):2300299.
51. Yao J, Lin R, Chen MK, Tsai DP. Integrated-resonant metadevices: a review Adv Photonics. 2023;5: 024001.
52. Jiang Q, Bao Y, Li J, Tian L, Cui T, Sun L, et al. Bi-channel near- and far-field optical vortex generator based on a single plasmonic metasurface. Photonics Res. 2020;8:986–94.
53. Berry MV. The adiabatic phase and Pancharatnam's phase for polarized light. J Mod Opt. 1987;34:1401–7.
54   Daniel S, Saastamoinen K, Saastamoinen T, Vartiainen I, Friberg AT, Visser TD. Surface plasmons carry the Pancharatnam-Berry geometric phase. Phys Rev Lett. 2017;119(25):253901.
55. Guo Y, Pu M, Zhang F, Xu M, Li X, Ma X, et al. Classical and generalized geometric phase in electromagnetic metasurfaces. Photonics Insights. 2022;1(1):R03.
56. Qu C, Ma SJ, Hao JM, Qiu M, Li X, Xiao SY, et al. Tailor the functionalities of metasurfaces based on a complete phase diagram. Phys Rev Lett. 2015;115:6.
57. Gerchberg RW, Saxton WO. A practical algorithm for the determination of phase from image and diffraction plane pictures. Optik. 1972;35:237–46.

Publisher's Note